Fast oxygen separation through SO2- and CO2- stable dual-phase membrane based on NiFe2O4- Ce 0.8Tb0.2O2-δ

4 AUTHORS, INCLUDING:

María Balaguer

Forschungszentrum Jülich

23 PUBLICATIONS   **161** CITATIONS

SEE PROFILE

Cecilia Solís

Universitat Politècnica de València

40 PUBLICATIONS   **418** CITATIONS

SEE PROFILE

Jose Manuel Serra

Universitat Politècnica de València

154 PUBLICATIONS   **2,322** CITATIONS

SEE PROFILE

Fast Oxygen Separation Through SO_2- and CO_2-Stable Dual-Phase Membrane Based on $NiFe_2O_4-Ce_{0.8}Tb_{0.2}O_{2-\delta}$

María Balaguer, Julio García-Fayos, Cecilia Solís, and José M. Serra*

Instituto de Tecnología Química (Universidad Politécnica de Valencia − Consejo Superior de Investigaciones Científicas), Av. Naranjos s/n, E-46022 Valencia (SPAIN)

S *Supporting Information*

ABSTRACT: Composite membranes with enhanced oxygen permeability and unprecedented stability in *oxyfuel*-like gas environments are reported. Specifically, 60 vol% $NiFe_2O_4$ - 40 vol% $Ce_{0.8}Tb_{0.2}O_{2-\delta}$ (NFO-CTO) composite has been successfully obtained by one-pot fabrication method showing both spinel and fluorite pure phases. Narrow grain size distribution centered around 1 μm and homogeneous distribution of grains is attained, as well as percolative pathways from side to side of the dual-phase membranes. The composite resisted a stability test in wet SO_2 and CO_2 containing gas at 800 °C for 170 h, which represents a step

forward toward its use in *oxyfuel* power plants. The conductivity of both phases is investigated as a function of temperature and oxygen partial pressure (pO_2). Oxygen separation in this kind of NFO-doped-ceria composite membranes occurs via the separate ambipolar transport through the two distinct percolating networks. Oxygen permeation flux values of 0.17 mL·min^{-1}·cm^{-2} and 0.20 mL·min^{-1}·cm^{-2} are achieved at 1000 °C when argon and pure CO_2 are used as sweep gas, respectively, through a 0.68 mm-thick membrane. Experiments at 900 °C showed that the material is stable and effective in pure CO_2 atmospheres and the oxygen permeation is even improved after 76 h on CO_2 stream.

KEYWORDS: *composite membrane, oxygen transport membrane, doped ceria, spinel composite, sulfur stable, terbium oxide*
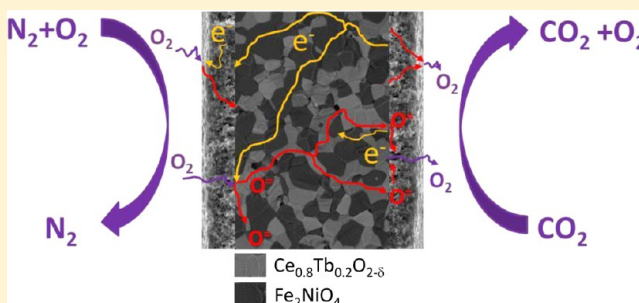
INTRODUCTION

Oxyfuel technology in different energy-demanding processes enables to reach important energy savings and facilitates the integration of CO_2 capture strategies that minimize greenhouse emissions. Oxyfuel technology consists of fuel combustion by using O_2 (instead of air) in a CO_2 sweeping stream. The absence of N_2 allows (i) more efficient combustion processes, (ii) minimizing NO_x formation, and (iii) the direct CO_2 sequestration process.[1] However, oxyfuel overall efficiency is penalized by the high energetic and economic costs associated with oxygen production using state-of-the-art cryogenic distillation units. The current alternatives for cryogenic air separation are modules based on oxygen transport membranes (OTMs), which may be thermally integrated in the furnace.[2] OTMs are made of mixed ionic electronic conductor (MIEC) materials that allow 100% oxygen selectivity.[3] Up to date, materials with perovskite structure are the MIEC materials showing the highest electrical conductivities but permeabilities are often limited by the ionic conductivity, thus jeopardizing the ambipolar conductivity.[3] Doping strategies to increase the oxygen ion conductivity normally affect the crystal and thermo-mechanical stability. This increases the vulnerability of the membrane when exposed to large oxygen concentration gradients and atmospheres containing CO_2, SO_2, and H_2O, that is, the operation conditions found in the oxyfuel process and catalytic membrane reactors in different intensified

industrial processes.[4−6] Improved stability against oxygen partial pressure gradients and carbonation is expected when avoiding the presence of alkaline-earth elements in the oxide lattice and doping by only transition metals and lanthanides instead.

The difficulty of joining all the desired characteristics in a single material pointed out to achieve them separately. Dual phase composite membranes try to combine the best characteristics of different compounds to achieve large oxygen permeability and relatively good chemical and mechanical stability at elevated temperatures. Thus, composite materials should consist of an electron conducting material, which allows the percolation of electrons and an ionic conductor that transports the oxygen ions through the membrane. Due to the existence of two phases, the influence of the grain boundary between them plays an important role, since it can either promote or block the transport of ionic and electronic species across the membrane. Furthermore, large catalytic activity toward surface oxygen exchange is required.

The first reported dual phase membranes were ceramic-metal (cermet) composites consisting of a continuous oxygen ion-conducting oxide phase and a continuous electron-conducting

noble metal phase,[7−9] but the high costs arising from the use of noble metals prevent the industrial applications. The total price may decrease by using ceramic−ceramic (cercer) dual-phase compounds, successfully prepared since early 2000′s decade.[10] In a cercer, other important requirements besides the transport properties have to be taken into account, that is, the stability of both phases against reaction with each other and the compatibility of thermal-chemical expansion of both compounds. Following this composite strategy, several crystalline structures have been combined, e.g. fluorites, perovskites, spinels and rock salts.[11] Materials with perovskite and spinel structure may be used as electronic phase.[12] Fluorite materials such as yttria stabilized zirconia (YSZ), stabilized bismuth oxide (SBO) or $Ce_{1−x}B_xO_{2−\delta}$ (B = lanthanide) play the oxygen conductor role in composites since they present mainly ionic conductivity. Moreover, the chemical stability of doped ceria is significantly higher than that of perovskites.[13] On these premises, cercers composed of doped ceria fluorites and several spinels have allowed the development of CO_2 stable composite membranes,[14,15] such as Co-free spinel $NiFe_2O_4$ (NFO) with $Ce_{0.9}Gd_{0.1}O_{1.95}$ (CGO10).[12]

In previous works, $Ce_{0.8}Tb_{0.2}O_{2−\delta}$ −2 mol % Co (CTO+Co) was reported to be a MIEC material at high oxygen partial pressures due to the variable oxidation state of the Tb.[16] The CTO+Co showed stability in CO_2 containing atmospheres, but the obtained oxygen fluxes were too low for a realistic application in industry due to the very low electronic conductivity of tested material. With the aim of improving the electronic conductivity of these membranes, NFO electronic phase has been added to the $Ce_{0.8}Tb_{0.2}O_{2−\delta}$ (CTO), by taking into account the similar TEC of both materials.

The present work reports the development of a CO_2 −SO_2 stable dual-phase material made of 60 vol.% NFO as electronic conductor and 40 vol.% CTO as oxide-ion conductor. A high amount of electronic phase has been selected in order to ensure the electronic percolation. Furthermore, the presence of mobile electronic charge carriers in CTO allows the formation of new additional electronic pathways. Therefore, the whole composite volume[17] is an electronic conductor, in contrast with the case of a simple ionic-electronic composite.

The characterization of powders and sintered membranes is carried out by X-ray diffraction (XRD) and scanning electron microscopy (SEM). The stability of the cercer material after 7 days treatment in a CO_2 and SO_2-containing wet gas environment at 800 °C was checked by XRD, Raman spectroscopy and SEM EDS microanalysis. An electrochemical study was performed by 4-point DC conductivity. Finally, the oxygen permeation of a planar disk dense membrane with both sides covered with a previously optimized catalytic composite layer was tested in argon and CO_2 sweeping gases.[18]

■ EXPERIMENTAL SECTION

The composite powder was prepared by *one pot method*, which allows the composite to be synthesized by a single step Pechini method.[12,19] This routine allows the enhancement of the oxygen flux with respect to solid state mixing method due to the improvement in morphology and homogeneity.[12,20]

Homogeneous solutions of each phase precursors (transition metals, M or lanthanides, Ln) are mixed in common solution and citric acid and ethylenglycol are added to form a complex. This complexation is followed by dehydration at low temperature and finally, the thermal decomposition of the precursors at 600 °C forms the structural phases (fluorite and spinel). Homogeneous-nanometric

sized grains are formed in a well-distributed mixture of the two phases forming the composite. Dense specimens are obtained by the 125 MPa uniaxial pressing of bars and green disks and subsequent calcination at 1350 °C for 5 h and 1400 °C for 10 h.

Identification of the crystalline phase and the lattice parameters of the samples were done by means of X-ray diffraction (XRD). The measurements were carried out by a PANalytical Cubix fast diffractometer, using $CuK\alpha_1$ radiation (λ = 1.5406 Å) and a X′Celerator detector in Bragg−Brentano geometry. XRD patterns recorded in the 2θ range from 10° to 90° were analyzed using X′Pert Highscore Plus software. The lattice parameter (a) was calculated by fitting reflection peaks to a Lorentzian function and using the equation for a cubic system.[21] SEM and EDX using a ZEISS Ultra55 field emission scanning electron microscope were used to analyze cross sections of the sintered material before and after the permeation test. Besides SEM backscattered electrons detector (BSD) was used to provide images with compositional contrast related to the averaged atomic number of the elements of each phase, and therefore different grains and element distribution to be distinguished. Renishaw inVia Raman spectrometer equipped with a Leica DMLM microscope measured Raman spectra, with a 514 nm Ar^+ ion laser. The depolarized beam was focused on a spot of about 3 μm by a ×50 objective of 8 mm optical length. A CCD array detector collected the Raman scattering.

The flue gas used for sweeping in oxyfuel processes may contain CO_2 and SO_2. The stability of the membrane material in similar harsh operation conditions was studied by XRD, SEM-EDS and Raman spectroscopy after treating the material during 7 days at 800 °C under a continuous flow consisted of CO_2 with 5% O_2 and 1% of SO_2 (water saturated gas at room temperature).

Electrical conductivity measurements were conducted by standard four-point DC technique on rectangular bars of 4 × 0.5 × 0.2 cm³, which were uniaxially pressed at 125 MPa and subsequently sintered for 5 h at 1400 °C in air. Silver wire and paste were used for contacting electrodes. The measurements were carried out after 2 h of stabilization at 800 °C by cooling down at a rate of 1 °C·min⁻¹ in constant O_2 containing atmospheres (Linde calibrated gas mixtures checked by a YSZ oxygen sensor). The constant current was supplied by a programmable current source (Keithley 2601) and the voltage drop through the sample was detected by a multimeter (Keithley 3706). The conductivity measurements are thermally activated and were analyzed on the basis of Arrhenius behavior $\sigma(T) = (A/T)\exp(−E_a/kT)$, from which the activation energy (E_a) is calculated.

Permeation tests were performed on a gastight composite disk sintered at 1400 °C. The thickness of the sample was 680 μm. Both disk sides were coated by screen printing a 30 μm layer of $Ce_{0.8}Gd_{0.2}O_{2−\delta}$-$La_{0.8}Sr_{0.2}MnO_{2−\delta}$ (CGO-LSM) ink, sintered and latter infiltrated using Pd nitrate solution, aiming to improve surface catalytic behavior. A gold gasket was employed for sealing the membrane. Oxygen was separated from synthetic air flow using argon and CO_2 as sweep gas. The total oxygen permeation rate fluxes (mL·min⁻¹·cm⁻²) were calculated assuming ideal gas law, as explained elsewhere. Permeate gas was analyzed using a micro-GC Varian CP-4900 equipped with Molsieve5A, PoraPlot-Q glass capillary, and CP-Sil modules. Appropriate sealing was confirmed by measuring the nitrogen tracer content of the permeate stream, which is only considered when it is lower than 5% of permeate. The permeation experimental standard deviation is $10^{−4}$. Besides, stability test against CO_2 was checked by exposing 100% CO_2 as sweep gas at 900 °C during 76 h. A complete time and temperature detail of the NFO-CTO dual-phase membrane permeation test is given in Supporting Information (SI) Figure S1. The membrane remained stable during two weeks in operation, including the use of CO_2 as sweep gas and repeated thermal cycling from 1000 to 650 °C, which did not cause any loss in mechanical integrity.

■ RESULTS AND DISCUSSION

The XRD pattern of 60%$NiFe_2O_4$-40%$Ce_{0.8}Tb_{0.2}O_{2−\delta}$ (NFO-CTO) sintered in air at 1400 °C is shown in Figure 1. For
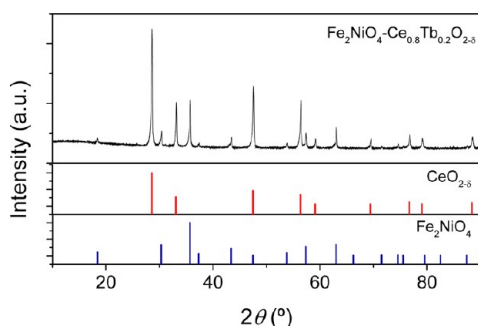
Figure 1. XRD patterns of the composite $NiFe_2O_4-Ce_{0.8}Tb_{0.2}O_{2-\delta}$ sintered in air at 1400 °C, compared with CeO_2 fluorite and Fe_2NiO_4 spinel structure.

comparison, also reference fluorite and spinel structure diffraction patterns are indicated (ICDD 00-043-1002 and 00-044-1485, respectively). Both structural phases are well-identified in the composite with no evidence of impurities or reaction between them up to the limit of the XRD device. The calculated cell parameters of the cubic spinel and the cubic fluorite (a = 8.332 Å and a = 5.406 Å, respectively) are very similar to those obtained for single phases separately (a = 8.339 Å and a = 5.392 Å, respectively), which point out that there is not interdiffusion of the elements. Diffusion of Ce or Tb inside the spinel structure (if any) should cause an expansion of the cell parameter, but the experimental data shows a slight shrinkage. On the other hand, the cell parameter of the ceria, which is longer than that observed previously for the single
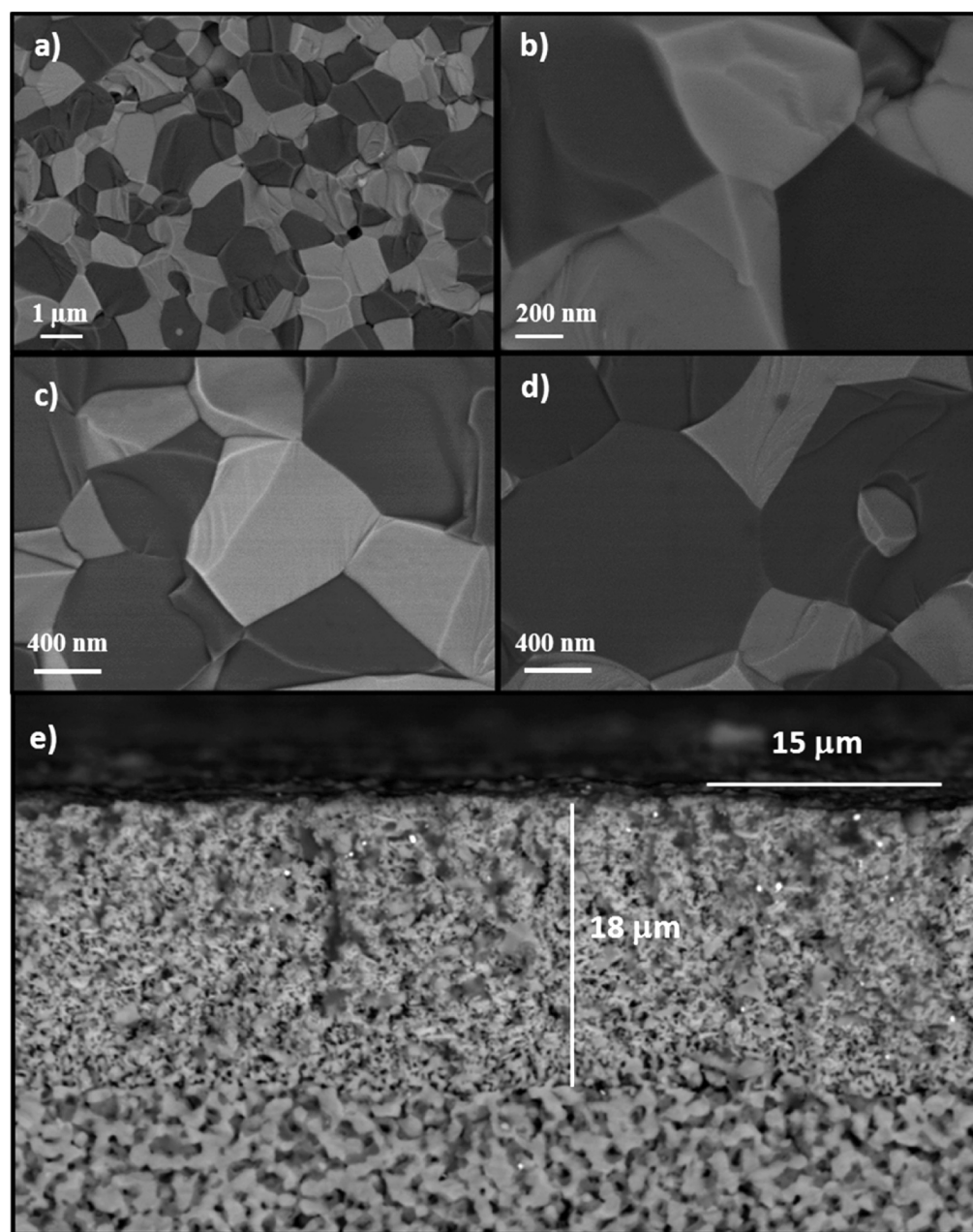

Figure 2. (a) SEM picture of the fractured cross-section of a 60%NFO-40%CTO composite membrane sintered at 1400 °C in air; (b) detail of the grain boundary between spinel (dark) and fluorite (light) phases; (c) detail of two fluorite grains fringe; (d) detail of two spinel grains fringe; and (e) CGO-LSM-Pd catalytic layer on the composite.
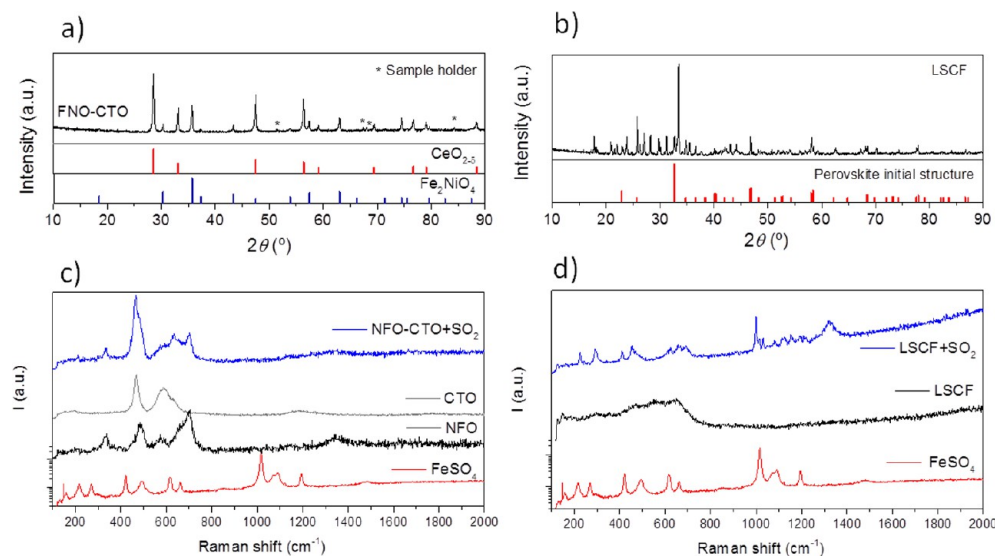
Figure 3. (a) XRD pattern of NFO-CTO composite and (b) LSCF after 7 days of treatment under a continuous flux consisted of 2.5% H_2O moistured 1% SO_2 −5% O_2 in CO_2, at 800 °C. (c) Raman spectra of NFO-CTO cercer after the same treatment compared with the as prepared single phases and $FeSO_4$. (d) Raman spectra of LSCF after and before the treatment and $FeSO_4$ spectra for comparison.
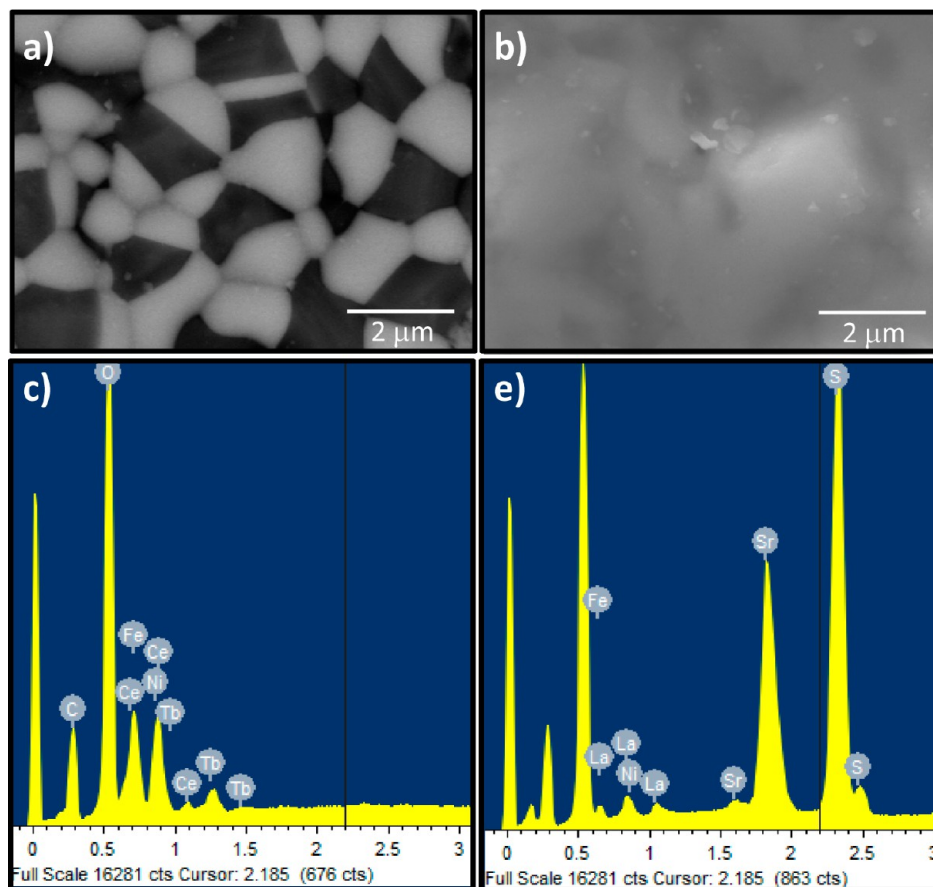

Figure 4. (a) FE-SEM backscattered image of (a) NFO-CTO composite membrane and (b) LSCF pellet after 7 days of treatment under a continuous flux consisted of 2.5% H_2O moistured 1% SO_2 −5% O_2 in CO_2, at 800 °C. (c) and (d) are the corresponding EDS analysis, respectively.

phase, could suggest that Tb dopant is not fully dissolved in the fluorite lattice, so that the rest should appear as Tb_2O_3 impurity. However, Tb_2O_3 was not detected by XRD. The composite was calcined in atmospheric air. Under such condition not all the Tb is introduced as Tb^{3+} (i.r. 1.04 Å) but as Tb^{4+} (i.r. 0.88 Å). Both the sample thermal history and

the influence of the spinel on the Tb reduction properties may cause the slight difference in the cell parameter by delivering higher ratio Tb^{3+}/Tb^{4+}.[22,23]

In Figure 2, the BSD-SEM images of a 1400 °C sintered NFO-CTO membrane show a dark phase that corresponds to the spinel and a bright one that belongs to the fluorite. In

Figure 2a, narrow grain size distribution (centered on 1 μm) and a homogeneous distribution of grains can be observed. Image analysis confirms the 60/40-volume phase ratio (spinel/fluorite). Figure 2b presents a higher magnification image offering details about the grain boundaries between the two different phases, and no phase reaction, impurities segregation or interdiffusion take place during the membrane sintering at 1400 °C. Further, Figure 2b−d reveal the very good bounding between grains made of the same phase (CTO-CTO or NFO-NFO) or different phases (NFO-CTO). Additionally, Figure 2e shows a detail of the 18 μm-thick CGO-LSM/Pd catalytic layer, which can be easily identified due to its smaller grain size and high porosity[18] and which will be discussed in detail later. The backscattered electrons image (Figure 2e) also makes visible the two distinct phases of this catalytic layer, that is, CGO corresponds to the bright phase and the LSM to the dark one. From this image, it is also visible a very clean interface between the membrane and the catalytic layer, with no reaction interfaces or cracks that reveals the chemical compatibility of all the different materials and the good bounding between the layer and the membrane.

The industrial application of the OTM may involve the presence of CO_2 and most probably SO_2 traces and moisture. Therefore, the stability of NFO-CTO composite was tested by treating the composite during 7 days at 800 °C under continuous flow of CO_2 with 5% O_2 and 1% of SO_2, saturated with 2.5% of H_2O. Then, the membrane surface exposed to this environment was analyzed by XRD and Raman spectroscopy (Figure 3) and by FE-SEM and EDS (Figure 4).

The XRD pattern plotted in Figure 3a reveals that, after the mentioned treatment, only spinel and fluorite phases appear and neither new oxide phases nor minor impurities are detected up to the limits of the diffractometer. On the contrary, the reference material $La_{0.8}Sr_{0.2}Co_{0.5}Fe_{0.5}O_{3-\delta}$ (LSCF) loses its perovskite structure when undergoes the same process (Figure 3b). This is confirmed by the Raman spectra of both materials depicted in Figure 3c and d for the composite and the LSCF, respectively. For comparison, the Raman spectra of CTO, NFO, $FeSO_4$, and LSCF single phases before the treatment are also depicted. The NFO-CTO composite shows the Raman spectra of both combined structures. Otherwise, LSCF spectrum matches that of $FeSO_4$ with just small traces of pristine structure.

Figure 4 shows SEM images of the composite (a) and the LSCF (b) pellets exposed to this harsh atmosphere, together with their respective EDS analysis (c and d). Electronic microscopy does not show any evidence of sulfur on the surface of the composite, while preserving the microstructure in contrast to the state of the art LSCF whose EDS presents intense peaks corresponding to sulfur atoms.

Once proved the compatibility between both crystalline phases, the appropriate microstructure of the sintered composite body and its preliminary stability in a CO_2 and SO_2 containing atmosphere, the transport properties were investigated. The NFO-CTO 60−40 vol.% ratio was selected in order to ensure the electronic percolation, which was the limiting mechanism in the CTO+Co single phase membrane.[17]

The plot in Figure 5a shows the electrical conductivity $\ln(\sigma T)$ as a function of reciprocal temperature recorded in air for the CTO and NFO single phases and for the composite. The composite conductivity is higher than the equivalent sum of the single components, which is attributed to the improved densification for the composite in contrast with the NFO with
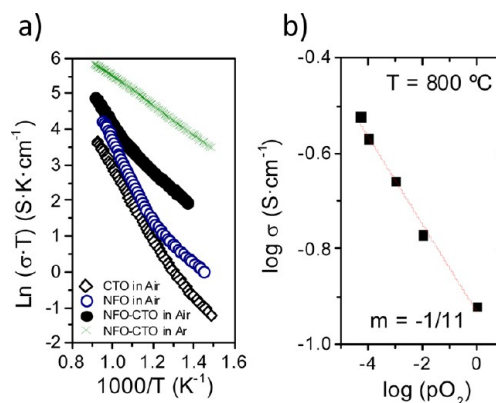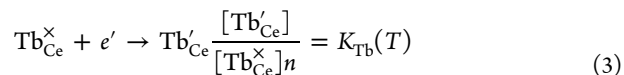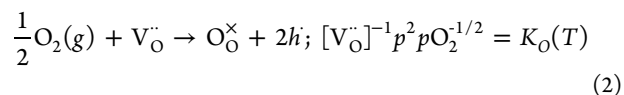

Figure 5. (a) Arrhenius plot of the total electrical conductivity in air for the single phase CTO, FNO and for the composite NFO-CTO in air and argon atmospheres and (b) logarithm total electrical conductivity at 800 °C as a function of the pO_2.

lower sintering activity. The NFO sintered sample was not totally dense when sintered at 1400 °C for 10 h (relative density ~84%, measured by Archimedes method), see SI Figure S2, whereas CTO and the composite are dense at the same conditions.[17]

An apparent change in the activation energy (E_a) is observed for the composite in air, which suggests a change in the dominant conduction mechanisms. E_a values of 0.45 and 0.71 eV have been calculated from the fitted data below and above 655 °C, respectively. The low temperature E_a may correspond to NFO phase and it is characteristic for the hopping of electronic charge carriers, that is, hopping of localized electrons between multivalent cations located in the octahedral Fe sublattice.[2]

$$Fe^{3+} + e' \rightarrow Fe^{2+} \tag{1}$$

For temperatures above 655 °C, oxygen is released from CTO phase (oxygen vacancy formation) and Tb^{4+} reduction to Tb^{3+} is induced,[17] which is charge compensated by the formation of electrons localized on Tb ions, as indicated by the following equations:

$$\frac{1}{2}O_2(g) + V_O^{\cdot\cdot} \rightarrow O_O^{\times} + 2h^{\cdot}; \; [V_O^{\cdot\cdot}]^{-1}p^2 pO_2^{-1/2} = K_O(T) \tag{2}$$

$$Tb_{Ce}^{\times} + e' \rightarrow Tb_{Ce}' \; \frac{[Tb_{Ce}']}{[Tb_{Ce}^{\times}]n} = K_{Tb}(T) \tag{3}$$

The oxygen vacancies concentration in combination with the strong thermal activation of the oxide ion mobility leads to the noticeable increase in the ionic conductivity. As a result, the contribution of the ionic transport to the total conductivity of the NFO-CTO composite becomes significant at temperatures above 655 °C. This thermal process in CTO is responsible for the raise in the overall composite E_a, which is related to the higher E_a associated to oxygen vacancy diffusion with regard to the electron hopping E_a observed at lower temperatures.[24]

Figure 5a also shows the electrical conductivity for the composite in argon ($pO_2 = 5 \times 10^{-5}$ atm) upon equilibration of the samples at 800 °C for 2 h. At this low pO_2, both phases of the composite are more reduced than in air, that is, terbium and iron cations are mainly reduced to Tb^{3+} and Fe^{2+} valence state along the whole studied temperature range. Hence, in argon, the concentration of oxygen vacancies in CTO remains

constant with decreasing temperatures. Consequently a monotonic Arrhenius behavior is observed, that is, E_a remains constant. The low E_a value (0.38 eV) suggests that the electronic conductivity of the partially reduced FNO governs the composite conductivity. Additionally, the conductivity increases substantially at higher temperatures due not only to the further activation of electron hopping rate but also to the increased probability of the localized electrons in the spinel to transfer from one ion to another due to the lattice vibrations. Thus, these trapped electronic carriers in the ferrite may contribute to the conduction process.

The total electrical conductivity of the composite at 800 °C is depicted in Figure 5c as a function of the pO_2. Nickel ferrite is a p or n-type semiconductor depending on the oxygen deficiency, which is in turn determined by the sintering temperature and atmosphere. The present sintering conditions, that is, high temperatures and oxygen partial pressures lower than 4 atm of oxygen, favor high Fe^{2+} concentrations instead of Ni^{3+} holes.[2,25] Thus, n-type conductivity ($pO_2^{-1/4}$ dependency) is expected. On the other hand, CTO ionic conductivity presents a $pO_2^{-1/6}$ dependency at high pO_2, which provokes the adjustment of the composite-pO_2 dependency to $pO_2^{-1/11}$, as shown in Figure 5c.[2]

The preceding results provide sufficient evidence about the participation of both ionic and electronic carriers in the ambipolar conduction, which are appropriate transport properties for the composite to work as OTM. In order to promote the oxygen activation on the membrane surface, a catalytic layer consisted of CGO-LSM porous composite (Figure 3e) and Pd infiltration was selected. In a previous work, this mixture demonstrated to be the optimum between LSM-doped ceria compositions with good electrochemical properties for oxygen activation at high temperatures, while these phases are known to be stable and effective in CO_2-rich atmospheres.[16] CGO provides the ionic conductivity that LSM lacks and thus allows (i) the global three-phase-boundary (TPB) region of the oxygen activation to be increased; and (ii) additional redox electrocatalytic activity to be incorporated. Besides, no reaction between the layer and the membrane surface was observed indicating their chemical compatibility.

The oxygen permeation through a 0.68 mm-thick NFO-CTO membrane was measured as a function of temperature by using two different sweeping gases, that is, argon and pure CO_2, as shown in Figure 6a. Taking the results at 1000 °C as reference data, oxygen fluxes of 0.17 mL·min^{-1}·cm^{-2} and 0.20

mL·min^{-1}·cm^{-2} were obtained for argon and CO_2 sweepings, respectively. These permeation values are about twice the permeation values achieved using a single phase Co-containing $Ce_{0.8}Tb_{0.2}O_{2-\delta}$ (CTOCo) membrane in similar conditions.[17] The result stresses the importance of the electronic contribution provided by the spinel percolating network that increases the ambipolar conductivity.

Figure 6a also shows that the use of CO_2 instead of argon as a sweep gas improves oxygen permeation at high temperatures (above 900 °C). This is ascribed to the better sweeping properties of CO_2 with respect to argon at these temperatures and to the smaller CO_2 adsorption constant as the temperature is increased, neglecting in this way the effect of competitive adsorption.[26−28] On the other hand, the CO_2 does affect the oxygen permeation at low temperature. The reduction in oxygen permeation can be due to either carbonate formation on behalf of the reaction with the membrane components or to O_2 competitive adsorption on the membrane surface. Since terbium doped ceria and NFO are not prone to interact with CO_2 to form carbonates,[12,17] the oxygen permeation drop observed in Figure 6a at temperatures below 900 °C is more likely related to the aforementioned $O_2−CO_2$ competitive adsorption on reaction sites. As previously observed on several oxygen-ion conductor surfaces, this process is more favorable as long as the temperature diminishes,[5,27] due to the exothermic nature of CO_2 adsorption.

Figure 6b represents the evolution of the oxygen permeation as a function of time in CO_2 sweeping conditions, at 900 °C. The flux kept stable during at least 76 h and slightly increased with time on stream. Although it is not a long-term test, it makes the difference between the Co-free composites and the broadly applied perovskite materials as BSCF or LSCF, which readily drop the oxygen flux when CO_2 gas is applied.[12,20,25,29,30] The origin of the intriguing permeation activation with time remains unclear and may be related with surface and/or grain boundary processes.

Finally, the membrane was compared with a composite made of 60% NFO and 40% CGO. This composite was selected as a reference since the CGO is a well-known ionic conductor at high oxygen partial pressures. Besides, a 40% NFO to 60% CGO membrane was reported to be CO_2 stable by Luo et al.[31] Figure 7a shows the permeation flux of NFO-CTO and NFO-CGO membranes prepared in an identical way, and their transport schemes are shown in Figure 7b and c, respectively. NFO-CTO composite membrane exhibits higher oxygen permeation, especially with decreasing temperatures, despite the lower ionic conductivity of CTO (see SI Figure S3). The improved behavior of the NFO-CTO membrane may originate from the higher p-type electronic conductivity of CTO,[17] which increases the overall mixed ionic-electronic conductivity of the composite to the overall CTO grain volume and does not block the electronic pathways in the bulk of the membrane. This is in contrast with the NFO-CGO composite since CGO behaves as a purely ionic conductor in the applied pO_2 environments and electronic carriers are blocked in the grain boundaries (Figure 7c).

In this work, predominance was given to provide electronic conductivity to a main ionic conductor as CTO. However, other composites have shown different optimum ratios for maximizing the oxygen permeation, that is, the ambipolar conductivity. First dual-phase membranes joining $Ce_{0.8}Gd_{0.2}O_{1.9}$ (CGO20) with $CoFe_2O_4$ (CFO) and $MnFe_2O_4$ (MFO) found that 30% volume of spinel phase
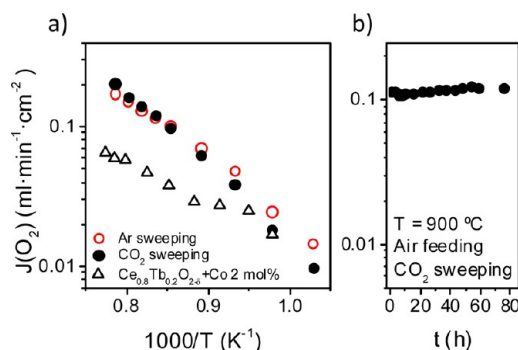

Figure 6. (a) Oxygen permeation flux as a function of temperature and sweep gas (argon or CO_2) for NFO-CTO membrane and for single phase CTOCo; and (b) flux stability with time on stream for NFO-CTO membrane in CO_2 at 900 °C.
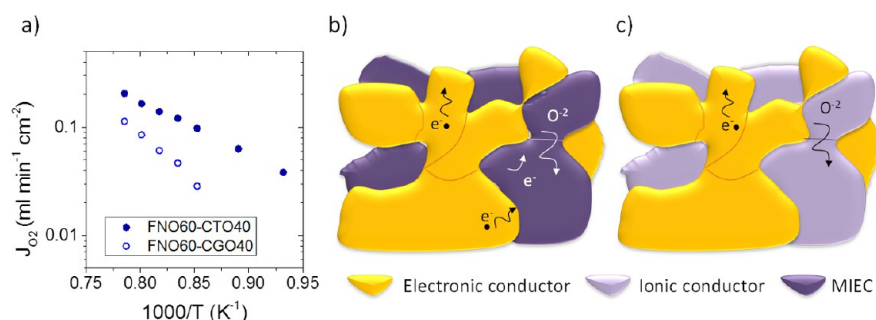
Figure 7. (a) Temperature dependency of oxygen permeation of NFO-CTO and NFO-CGO composites. The membranes were fed by air and the sweep gas was 100% CO_2, (b) schematic representation of the charge transport in a MIEC-electronic conductor composite, and (c) in a ionic conductor- electronic conductor composite.

was the optimum although lower fractions of spinel (ca. 17%) are also oxygen permeating.[15,32] Therefore, the optimization of the NFO-CTO ratio is expected to deliver higher oxygen permeation rates, while being stable in CO_2 and SO_2 containing environments.

CONCLUSIONS

One-pot fabrication of $60\%NiFe_2O_4$-$40\%Ce_{0.8}Tb_{0.2}O_{2-\delta}$ (NFO-CTO) composite was successfully obtained delivering both spinel and fluorite pure phase materials. No evidence of impurities or reaction between them is found up to the limits of the XRD. Additionally, SEM analysis reveals a narrow grain size distribution, homogeneous distribution of grains and good packing and bounding among the different grains in the membrane. Raman, XRD and EDS taken after a preliminary stability test demonstrated that NFO-CTO resists in a SO_2 and CO_2 environment without reaction either with the gases or between component materials.

The conductivity of both phases was investigated as a function of temperature and oxygen partial pressure (pO_2). The ambipolar transport involves the concomitant (i) hopping of charge carriers, that is, hopping of localized electrons between multivalent cations located in the octahedral Fe sublattice and (ii) the ionic transport in though the doped ceria lattice. Additionally, CTO presents significant p-type electronic conductivity although the ionic conductivity prevails.

Oxygen permeation flux values of 0.17 mL·min^{-1}·cm^{-2} and 0.20 mL·min^{-1}·cm^{-2} are measured through a 0.68 mm-thick membrane at 1000 °C when argon and pure CO_2 are used as sweep gas, respectively. Experiments at 900 °C showed that the material is CO_2 stable and the oxygen permeation is even improved after 76 h on stream.

Conclusively, the unprecedented chemical stability of the NFO-CTO composite and reasonable oxygen fluxes turns it an appealing material for oxygen separation integrated in oxyfuel processes using recirculated flue gas as sweep and in high-temperature catalytic membrane reactors.

ASSOCIATED CONTENT

Ⓢ Supporting Information

Additional information as noted in the text. This material is available free of charge via the Internet at http://pubs.acs.org.

AUTHOR INFORMATION

Corresponding Author

*Tel. +34.963.879.448. Fax: +34.963.877.809. E-mail: jmserra@itq.upv.es.

Notes

The authors declare no competing financial interest.

ACKNOWLEDGMENTS

REFERENCES

(1) MacDowell, N.; Florin, N.; Buchard, A.; Hallett, J.; Galindo, A.; Jackson, G.; Adjiman, C. S.; Williams, C. K.; Shah, N.; Fennell, P. *Energy Environ. Sci.* **2010**, *3*, 1645.

(2) Badwal, S. P. S.; Ciacchi, F. T. *Adv. Mater.* **2001**, *13*, 993.

(3) Sunarso, J.; Baumann, S.; Serra, J. M.; Meulenberg, W. A.; Liu, S.; Lin, Y. S.; da Costa, J. C. D. *J. Membr. Sci.* **2008**, *320*, 13.

(4) Pilar Lobera, M.; Escolastico, S.; Garcia-Fayos, J.; Serra, J. M. *Chemsuschem* **2012**, *5*, 1587.

(5) García-Torregrosa, I.; Lobera, M. P.; Solís, C.; Atienzar, P.; Serra, J. M. *Adv. Energy Mater.* **2011**, *1*, 618.

(6) Stadler, H.; Beggel, F.; Habermehl, M.; Persigehl, B.; Kneer, R.; Modigell, M.; Jeschke, P. *Int. J. Greenhouse Gas Control* **2011**, *5*, 7.

(7) Mazanec, T. J.; Cable, T. L.; Frye, J. G. *Solid State Ionics* **1992**, *53*, 111.

(8) Chen, C. S.; Burggraaf, A. J. *J. Appl. Electrochem.* **1999**, *29*, 355.

(9) Chen, C. S.; Kruidhof, H.; Bouwmeester, H. J. M.; Verweij, H.; Burggraaf, A. J. *Solid State Ionics* **1996**, *86–8*, 569.

(10) Nigge, U.; Wiemhofer, H. D.; Romer, E. W. J.; Bouwmeester, H. J. M.; Schulte, T. R. *Solid State Ionics* **2002**, *146*, 163.

(11) Shaula, A. L.; Kharton, V. V.; Marques, F. M. B.; Kovalevsky, A. V.; Viskup, A. P.; Naumovich, E. N. *J. Solid State Electrochem.* **2006**, *10*, 28.

(12) Luo, H.; Efimov, K.; Jiang, H.; Feldhoff, A.; Wang, H.; Caro, J. *Angew. Chem., Int. Ed.* **2011**, *50*, 759.

(13) Yi, J.; Zuo, Y.; Liu, W.; Winnubst, L.; Chen, C. *J. Membr. Sci.* **2006**, *280*, 849.

(14) Takamura, H.; Okumura, K.; Koshino, Y.; Kamegawa, A.; Okada, M. *J. Electroceram.* **2004**, *13*, 613.

(15) Takamura, H.; Kobayashi, T.; Kasahara, T.; Kamegawa, A.; Okada, M. *J. Alloys Compd.* **2006**, *408–412*, 1084.

(16) Balaguer, M.; Yoo, C.-Y.; Bouwmeester, H. J. M.; Serra, J. M. *J. Mater. Chem. A* **2013**, *1*, 10234.

(17) Balaguer, M.; Solis, C.; Serra, J. M. *Chem. Mater.* **2011**, *23*, 2333.

(18) Balaguer, M.; Vert, V. B.; Navarrete, L.; Serra, J. M. *J. Power Sources* **2013**, *223*, 214.

(19) Serra, J. M.; Vert, V. B.; Betz, M.; Haanappel, V. A. C.; Meulenberg, W. A.; Tietz, F. *J. Electrochem. Soc.* **2008**, *155*, B207.

(20) Luo, H.; Jiang, H.; Efimov, K.; Caro, J.; Wang, H. *AIChE J.* **2011**, *57*, 2738.

(21) Kumar, A.; Babu, S.; Karakoti, A. S.; Schulte, A.; Seal, S. *Langmuir* **2009**, *25*, 10998.

(22) Balaguer, M.; Solis, C.; Serra, J. M. *J. Phys. Chem. C* **2012**, *116*, 7975.

(23) Shannon, R. D. *Acta Crystallogr., Sect. A: Found. Crystallogr.* **1976**, *32*, 751.

(24) Shluger, A. L.; Stoneham, A. M. *J. Phys.: Condens. Matter* **1993**, *5*, 3049.

(25) Lobera, M. P.; Escolástico, S.; Garcia-Fayos, J.; Serra, J. M. *ChemSusChem* **2012**, *5*, 1587.

(26) Tan, X.; Liu, N.; Meng, B.; Sunarso, J.; Zhang, K.; Liu, S. *J. Membr. Sci.* **2012**, *389*, 216.

(27) Vert, V. B.; Serra, J. M. *J. Power Sources* **2011**, *196*, 4270.

(28) Serra, J. M.; Garcia-Fayos, J.; Baumann, S.; Schulze-Küppers, F.; Meulenberg, W. A. *J. Membr. Sci.* **2013**, *447*, 297.

(29) Benson, S. J.; Waller, D.; Kilner, J. A. *J. Electrochem. Soc.* **1999**, *146*, 1305.

(30) Schulz, M.; Kriegel, R.; Kaempfer, A. *J. Membr. Sci.* **2011**, *378*, 10.

(31) Luo, H.; Efimov, K.; Jiang, H.; Feldhoff, A.; Wang, H.; Caro, J. *Angew. Chem., Int. Ed.* **2011**, *50*, 759.

(32) Takamura, H.; Okumura, K.; Koshino, Y.; Kamegawa, A.; Okada, M. *J. Electroceram.* **2004**, *13*, 613.

4993

dx.doi.org/10.1021/cm4034963 | *Chem. Mater.* 2013, 25, 4986−4993